Experimental Evidence of Near-Wall Reverse Flow Events in a Zero Pressure Gradient Turbulent Boundary Layer

C. E. Willert[a,*], C. Cuvier[b], J. M. Foucaut[b], J. Klinner[a], M. Stanislas[b], J. P. Laval[b], S. Srinath[b], J. Soria[c,d], O. Amili[c,e], C. Atkinson[c], C. J. Kähler[f], S. Scharnowski[f], R. Hain[f], A. Schröder[g], R. Geisler[g], J. Agocs[g], A. Röse[g]

[a] *German Aerospace Center (DLR), Institute of Propulsion Technology, Measurement Technology, Linder Höhe, D-51147 Köln, Germany*
[b] *LML FRE3723, Univ. Lille, Centrale Lille, CNRS, Villeneuve d'Ascq, France*
[c] *Laboratory for Turbulence Research in Aerospace & Combustion (LTRAC), Department of Mechanical and Aerospace Engineering, Monash University (Clayton Campus), VIC 3800, Australia*
[d] *Department of Aeronautical Engineering, King Abdulaziz University, Jeddah, Kingdom of Saudi Arabia*
[e] *Department of Aerospace Engineering and Mechanics, University of Minnesota, Minneapolis, MN, USA*
[f] *Institut fur Strömungsmechanik und Aerodynamik LRT-7, Universität der Bundeswehr München, 85577 Neubiberg, Germany*
[g] *German Aerospace Centre (DLR), Institute of Aerodynamics & Flow Technology, Göttingen, Germany*

Abstract

This study reports on experimentally observed rare near-wall reverse flow events in a fully developed turbulent flat plate boundary layer at zero pressure gradient with Reynolds numbers between $Re_\theta \approx 2500$ and $Re_\theta \approx 8000$ ($Re_\tau \approx 800 - 2400$). The reverse flow events are captured using high magnification particle image velocimetry sequences with record lengths varying from 50 000 to 126 000 samples. Time resolved particle image sequences allow singular reverse flow events to be followed over several time steps whereas long records of nearly statistically independent samples provide a variety of single snapshots at a higher spatial resolution. The probability of occurrence lies in the order of 0.012 – 0.018% which matches predictions from direct numerical simulations (DNS). The typical size of the reverse flow bubble is about 30 wall units in length and 5 wall units in height which agrees well with similar observations made in existing DNS data.

Keywords: particle image velocimetry, turbulence statistics, boundary layer, flow reversal, wall shear stress
PACS: 47.80.-v 47.80.Jk 47.20.Ib 47.27.nb

*Corresponding author
Email address: chris.willert@dlr.de (C. E. Willert)

1. Introduction

The occurrence of near wall flow reversal and with it the presence of negative values of the local wall shear stress τ_w of turbulent boundary layers (TBL) have been subject of debate over the past decades. Eckelmann [1] postulated that near wall reverse flow was not possible and experimentalists have rarely, if at all, observed this somewhat counter-intuitive flow phenomenon. On the other hand a variety of direct numerical simulations (DNS) suggest the opposite. For DNS of zero pressure gradient turbulent boundary-layers (ZPG TBL) events of negative shear stress have been reported by Spalart and Coleman [2] and also for a turbulent channel flow by Hu et al. [3]. Similar observations have been made by Lenaers et al. [4] using simulations of turbulent channel flow as well as ZPG TBL up to shear Reynolds numbers of $Re_\tau = u_\tau\,\delta/\nu = 1000$. Negative wall shear stress events are also documented in turbulent pipe flow [5]. Cardesa et al. [6] also confirm the existence of areas of vanishing wall shear stress in DNS of turbulent channel flow at $Re_\tau = 934$ and $Re_\tau = 1834$ and associate these so-called critical points with large scale structures that extend up to 800 wall units downstream. More recently reverse flow events have been characterized through DNS in the adverse pressure gradient (APG) region on the suction side of an airfoil [7].

Common to the observations of the DNS data is that with increasing Reynolds number both the occurrence and the magnitude of the negative axial/streamwise velocities increase. Lenaers et al. [4, 7] report reverse flow occurrence of 0.01% for $Re_\tau = 180$ increasing to 0.06% for $Re_\tau = 1000$. In their DNS of fully turbulent channel flow Hu et al. [3] report a probability of negative wall shear ($\tau_w < 0$) of 0.003% at $Re_\tau = 90$ increasing to 0.085% at $Re_\tau = 1440$.

Due to their predicted low occurrence reverse flow phenomena have only been observed rather seldom in experiments involving ZPG wall bounded flows. To properly capture these events long records are necessary which until recently has only been possible for single point techniques, for instance through the use of laser Doppler velocimetry in a ZPG TBL as reported by Johansson [8]. At the same time the employed measurement technique needs to provide adequate spatial resolution as the reverse flow structures observed in DNS data are both short-lived and restricted to the viscous sublayer ($O(5y^+)$). Using the micro pillar shear stress imaging technique, Brücker [9] has recently been able to visualize the areas of reverse flow on a flat plate turbulent boundary layer at $Re_\tau \approx 940$.

Flow topology can nowadays be obtained through particle image velocimetry (PIV), yet, in comparison to single point techniques, PIV is generally restricted in acquisition frequency, number of samples and measurement uncertainty. This can be partially overcome by restricting the camera field of view which allows both an increase of sample rate and sample count [10]. The following reports on PIV measurements in the near wall area of a TBL with a negligible pressure gradient using sample counts exceeding 100 000 which is shown to be sufficient to capture several instance of reverse flow events.

The PIV measurements were primarily conducted to characterize the upstream conditions for a different experiment performed further downstream within the 20 m long test section [11]. Long records, some of which are temporally resolved, enable the capture of rare events such as those described here.

2. Wind tunnel facility

The measurements were performed at the turbulent boundary layer wind tunnel at the Laboratoire de Mécanique de Lille (LML). The measurement positions are located at $X = 3.2\,\mathrm{m}$ and 6.8 m downstream of the boundary layer trip position which is chosen as the origin of the coordinate system with the X-axis aligned in the streamwise direction, Y is the wall-normal and Z the spanwise direction. The tripping device is located at the junction between the contraction nozzle and the $2 \times 1\,\mathrm{m}^2$ rectangular test section and consists of a 4 mm rod attached to the tunnel wall followed by a 93 mm wide strip of coarse sandpaper (roughness 40-grit). Full optical access to the 20 m long rectangular test section is provided by large glass windows on all four sides.

Data was acquired at two free stream velocities of $U_\infty = 5\,\mathrm{m/s}$ and $U_\infty = 9\,\mathrm{m/s}$ with the wind tunnel velocities stable to within 0.5%. Temperature stabilization was set at $20.0 \pm 0.1\,^\circ\mathrm{C}$. Table 1 provides the relevant parameters of the turbulent boundary layer at the specific measurement conditions. The friction velocity can be retrieved directly from the PIV measurements using the methodology described in [10]. Other parameters such as the boundary layer thickness are partly estimated from theory (shown in parentheses) since at $X = 3.2\,\mathrm{m}$ only the lower portion of boundary layer was captured by the high resolution PIV measurements. The pressure distribution obtained from discrete positions along the centerline of the tunnel top wall is presented in Fig. 1 and exhibits a small, favorable pressure gradient due to the acceleration of the flow by the growing boundary layers on all four sides of the test section.

The recovered data is normalized with inner variables using the traditional viscous scaling for velocity $u_i^+ (= u_i/u_\tau)$, length $l_i^+ (= l_i\, u_\tau/\nu)$, and time $t^+ (= tu_\tau^2/\nu)$ with u_τ being the friction velocity and ν the kinematic viscosity.

3. PIV measurement and data-processing

Two PIV measurement configurations were used to characterize the turbulent boundary layer. Stereoscopic PIV captured all three velocity components in a spanwise wall-normal plane located at $X = 6.8\,\mathrm{m}$ downstream of the tripping device. The field of view covered is 300 mm in spanwise direction and 180 mm in wall normal direction and covers the full height of the boundary layer. A second PIV imaging setup was aimed at capturing the flow field in the immediate vicinity of the wall at a higher magnification. Following the procedures described by Willert [10] only a narrow wall-normal strip was imaged by the PIV camera, primarily to obtain the wall-normal velocity profile and related higher order statistics. For these measurements the plane is aligned in a streamwise wall-normal direction of about 5 mm width and 20 mm height.

Table 1: Global parameters of the boundary layer experiments with estimated values given in parenthesis

measurement location	X	[m]	3.2	3.2	6.8	6.8
free stream velocity	U_∞	[m s^{-1}]	5.0	(9.0)	5.0	9.0
local free stream velocity	U_e	[m s^{-1}]	(5.2)	(9.3)	5.4	9.6
boundary layer thickness	δ_{99}	[mm]	(59)	(54)	109	102
displacement thickness	δ^*	[mm]	(10.4)	(9.0)	18.5	16.9
momentum thickness	θ	[mm]	(7.4)	(6.5)	13.4	12.4
shape factor	$H_{12} = \delta^*/\theta$		(1.405)	(1.376)	1.381	1.359
wall shear rate	$\dot{\gamma} = \partial u/\partial y\|_0$	[s]$^{-1}$	2990	8620	2750	8100
friction velocity	u_τ	[m s^{-1}]	0.213	0.362	0.204	0.350
friction coefficient	c_f		(0.00333)	(0.00303)	0.00288	0.00262
pressure gradient	$\partial p/\partial x$	[Pa/m]	-0.17	-0.42	-0.17	-0.42
	$\partial p/\partial x^+$	$\times 10^4$	-2.5	-1.2	-2.5	-1.2
momentum Reynolds number	$Re_\theta = U_e\,\theta/\nu$		(2537)	(4000)	4767	7952
shear Reynolds number	$Re_\tau = u_\tau\,\delta_{99}/\nu$		(825)	(1293)	1477	2374
wall unit	$l^* = \nu/u_\tau$	μm	71.3	42.0	74.1	43.2

For high magnification PIV, two camera types were used to capture the long image sequences. A high-speed CMOS camera with 36 GB of RAM (Dimax-S4, PCO GmbH, Germany) captured more than 126 000 frames at 6.7 kHz to provide continuous time records. By reducing sample rates to 1-2 kHz statistical independence of the samples was improved while maintaining a similar sample count. Additional measurements were performed using a scientific CMOS PIV camera (Edge 5.5, PCO GmbH, Germany) which featured increased sensitivity and higher spatial resolution. This camera was operated at a double frame rate of 200 Hz to capture long records of statistically independent samples.

The roughly 5 mm wide measurement area was illuminated by a pair of externally modulated continuous wave lasers (Kvant Laser, Slovakia) with a combined output power of about 10 W at a wavelength of 520 nm. The non-collimated laser beam with a size of about 6×2 mm^2 was focussed into a uniform 6 mm wide light sheet using a cylindrical lens with focal length of 200 mm. The resulting waist thickness was on the order of 200 μm before entering the wind tunnel glass panel from below.

Seeding was provided globally in the closed circuit wind tunnel. Consisting of an evaporated-recondensed water-glycol mixture, it was introduced in the diffuser downstream of the 20 m long test section just upstream of the fan. The size of the aerosol droplets is estimated at 1μm with a lifetime in the order of 10 minutes.

To provide a sufficiently high magnification at a working distance of ≈ 1.1 m to the tunnel's centerline, a telephoto lens (Zeiss Apo-Tessar 300 mm/f2.8) with a 100 mm extension tube imaged the near wall region with a magnification of $m = 0.44$. The high-speed camera has a pixel size of 11 μm which corresponds to a magnification of 25.4 μm per pixel in object space. For the sCMOS camera, with 6.5 μm pixel pitch, the spatial resolution improves to 14.1 μm per pixel. In terms of viscous scaling the camera resolution varied from 1.6 to 5.2 pixel per

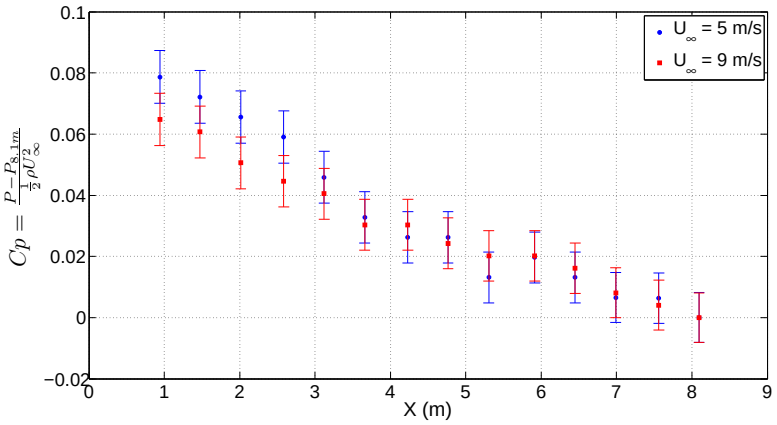

Figure 1: Streamwise pressure coefficient distribution on the wind tunnel top wall for the two studied free stream velocities with respect to pressure measurement at $X = 8.1\,\mathrm{m}$.

Table 2: PIV parameters of the boundary layer experiments

Camera model			**PCO Dimax-S4**	**PCO Edge 5.5**
pixel size		[μm^2]	11.0×11.0	6.5×6.5
magnification	m	[μm pixel^{-1}]	25.4	14.1
image size	$H \times W$	[pixel]	200×1008	200×2560
field of view	$w \times h$	[mm^2]	5.08×25.6	2.82×36.1
pulse separation	at 5 m/s	[μs]	150	100
	at 9 m/s	[μs]	100	65

wall unit. To make use of nearly the full aperture of the objective lens the optical axis was inclined about 2° with respect to the tunnel wall. At this angle the $200\,\mu$m thin light introduced through the windtunnel window has a projected thickness of about $7\,\mu$m (0.25 – 0.5 pixel). Therefore, only a minor perspective error is introduced by the spanwise distribution of particles illuminated by the thin light sheet.

The acquired data was processed using a conventional 2-C PIV processing package featuring a coarse-to-fine resolution pyramid with intermediate image deformation (PIVview2C, PIVTEC GmbH, Germany). To obtain reliable mean velocity data and statistics within close proximity to the wall a high aspect ratio image sampling window of 64 pixels in streamwise and 6 pixels in wall-normal direction was chosen. This corresponds to $1.63 \times 0.15\,\mathrm{mm}^2$ for the high-speed camera and $0.90 \times 0.08\,\mathrm{mm}^2$ for the sCMOS camera. For the latter, the sample has an effective size of $12.6\,x^+ \times 1.2\,y^+$ at $U_\infty = 5\,\mathrm{m/s}$ increasing to $21.1\,x^+ \times 2.0\,y^+$ at $U_\infty = 9\,\mathrm{m/s}$. For the detailed investigation of specific

reverse flow events the PIV sample window was further reduced to 24×8 or 32×6. The sample overlap varied between 67% and 75%.

Estimates of the mean and unsteady wall shear rate $\dot{\gamma} = \partial u/\partial y$ were obtained using a single-line cross-correlation approach. In this case the sampling window has a wall-normal size of only one pixel, which only recover the horizontal displacement.

4. Data analysis

To verify that the investigated flow is representative for a ZPG TBL the following describes some relevant statistics retrieved from the processed data sets. In this sense the normalized mean streamwise velocity profiles at position $X = 6.8\,\mathrm{m}$ for both Reynolds numbers are shown in Fig. 2 along with the corresponding variances $\langle u'u' \rangle$, $\langle v'v' \rangle$ and covariances $\langle u'v' \rangle$. Both plots also contain reference data from DNS and LES of a ZPG TBL respectively provided by Sillero et al. [12] and Eitel-Amor et al. [13]. For the most part, the agreement between experiment and simulation is very good (the lines practically overlap). Due to the limited field of view, the outer region of the boundary layer ($y^+ > 400$) is not captured by the high magnification PIV setup. Discrepancies can be observed very close to the wall for the high-Re case and can be attributed the loss of resolution proportional to the reduction in viscous length scales at increasing Reynolds numbers. Due to the coarser resolution of the conventional stereo PIV imaging setup, reliable measurements are only possible for wall distances greater than $y^+ = 100$.

Characteristic quantities such as the skin-friction coefficient c_f and the shape factor H_{12} listed in Table 1 respectively are within 5% and 1% of the values suggested by Chauhan et al. [14].

Making use of the high spatial resolution near the wall, both the mean and unsteady wall shear rate $\dot{\gamma} = \partial u/\partial y$ and with it the corresponding wall shear stress $\tau_w = \mu\, \partial u/\partial y$ can be directly estimated from the velocity gradient at the wall. Here the reader is referred to [10] for details on the processing scheme. Fig. 3 shows the probability density functions (PDF) of the wall shear stress τ_w extracted from several of available image sequences, which show good agreement with data published in literature [15, 3, 16, 4, 17]. The vertical dashed line marks the position for $\tau_w = 0$. When plotted in log-linear form the PDF of the shear stress exhibits instances of negative shear stress with a probability of less than 0.1%. Since the wall shear stress is directly related to the near-wall velocity, the PDFs of the streamwise velocity u at wall distances of $1\,y^+$ and $5\,y^+$ are provided in Fig. 4. Here it can be observed that the reverse flow seems to only appear very close to the wall while it is practically absent outside of the viscous sublayer for $y > 5\,y^+$.

At this point it should be noted that the data in the tails of the PDFs have an increasing likelihood of being affected by measurement errors (outliers) rather than representing reliable measurements. Therefore, the underlying data sets require separate verification to determine a given datum's validity, which, taking into account the rather low probability of less than 0.1%, is feasible

through visual inspection of the data. This can be achieved through velocity-vs-time plots such as shown in Fig. 5. This image is compiled by extracting a single column of data from each PIV data set of the sequence and placing the columns side-by-side such that the resulting image has a width of up to 126 000 pixels, depending on the number of samples within a given data set. Therefore, each horizontal line of pixels in the image represents the velocity record for a given wall distance.

Reverse flow events can be easily detected by highlighting negative velocities in images such as Fig. 5 and retrieving the corresponding single data sets from the sequence for closer inspection. One such event is the white spot near the middle of the bottom edge of Fig. 5. The spot is about 5 wall units high with a duration of about $t \approx 7\,t^+$, the former giving an indication on the vertical height of the reverse flow bubble (i.e. about 300μm). In the present sequence of 126 000 images only two such reverse flow events can be detected. Taking into account the duration of about 10-15 samples per event results in a probability of about 0.01%. Analysis of the statistically independent sampled image sequences show between 8 and 12 reverse flow events on record lengths of nearly 64 000 samples, corresponding to a probability of 0.012 – 0.018%.

As the image sequences are temporally well resolved, the evolution of a specific reverse flow event can be observed within the narrow field of view. In this sense the particle tracks, compiled through the summation of several images, visualize the shape of the flow structure (Fig. 6). Another way of visualising the reverse flow phenomenon is shown in Fig. 7 which captures the streamwise motion of particles at four different wall distances for a duration of 0.1 s (667 images). These space-time particle tracks are assembled by extracting a single fixed row of pixels from each image of the sequence. Particle tracks with a steep slope indicate slow moving particles; those at rest exhibit a pure vertical slope. Near time $t = 0$ the particle tracks exhibit an S-shaped motion at wall distances $y = 1.2\,y^+$ and $y = 3.8\,y^+$, which indicate their brief motion in an upstream direction. At a wall distance of $y = 7.5\,y^+$ the particles briefly come to rest and a flow reversal is not as obvious. At greater wall distances – here $y = 14.9\,y^+$ – there is no indication of flow reversal.

Magnified views of the flow field surrounding two reverse flow events are provided in Fig. 8 at two different Reynolds numbers. The thick contour near the wall at $Y = 0$ encloses the area with negative streamwise velocity $u < 0$. To highlight the flow topology additional plots are provided with the mean local velocity subtracted. The passage of the reverse flow region through the field of view is shown by a sequence of velocity fields in Fig. 9 for which only every fourth frame is shown. Finally snapshots of several different "separation bubbles" are shown in Fig. 10 for the upstream measurement location at $X = 3.2$ m and free stream velocities of $U_\infty = 5$ m/s and $U_\infty = 9$ m/s.

5. Results and discussion

In total eight sequences at two measurement locations and two free stream velocities were investigated for the presence of reverse flow. While some se-

quences were affected by low seeding density and limited spatial resolution, all sequences show multiple incidences of reverse flow in the form of particles moving upstream for a certain duration. The appearance of the flow features has a probability of $1.2 - 1.8 \times 10^{-4}$.

In most cases the reverse flow region has a vertical dimension of $5\,y^+$ and a length of about $30\,x^+$ which is consistent with the DNS results provided by Lenaers et al [4] (e.g. see Fig. 8 in their publication). Time-resolved sequences show that the "separation bubble" traverses downstream through the field of view at a convection speed U_c of about $0.1\,U_e$ or $U_c/u_\tau \approx 2.5$ (estimated from Fig. 9) which corresponds to the mean velocity of the viscous sublayer. While not captured through the present measurements, the corresponding DNS indicate that the structures have a spanwise dimension on the order of $30\,z^+$, that is, their xz shape is roughly circular. Although the number of samples is limited the flow field surrounding the "separation bubble" can be considered to be self similar, in particular when plotted in fluctuating velocity (mean local velocity subtracted). The reverse flow is associated with a local deceleration of the flow of up to $8\,U^+$ extending well into the buffer layer. Contrary to the mean velocity profile, the local velocity profile exhibits an inflection point within the buffer layer (i.e. $y > 10\,y^+$). When plotted in fluctuating velocity a vortical structure is present above the reverse flow patch within the buffer layer. This was also reported by Lenaers et al [4] who state that the backflow is induced by strong oblique vortices located above. These oblique vortex structures are believed to be a result of streak instabilities in the turbulent boundary layer [18].

Aside from the rare occurrence of the reverse flow events the DNS results by Lenaers et al [4] indicate that they appear quite sudden. While the number of events captured with PIV are too few to allow for a statistical analysis, the passage of the reversed flow structure through the field of view as in Fig. 9 suggests a persistence on the order of 3 ms or $t \approx 10\,t^+$. Here the question arises whether the particles used to visualize the events can faithfully follow the flow. The water-glycol droplets used in this investigation have a diameter of about 1μm and a relaxation time $\tau \approx 10\,\mu$s or $t \approx 0.03\,t^+$. In the viscous sublayer the Stokes number $St = \tau\,U\,d^{-1}$ based on friction velocity u_τ and viscous sublayer thickness $d = 5\,y^+$ reduces to 0.005, which indicates that the particles can faithfully follow the flow reversal events.

6. Summary and outlook

Through analysis of long PIV data sequences rare events such as small-scale near wall flow reversal could be documented at two measurement locations and two free stream velocities of a ZPG TBL. Both the probability of occurrence as well as the shape of the observed reverse flow structures agree with previous DNS by Lenaers et al [4]. Similar reverse flow events could also be observed in time-resolved, high resolution 3-D PTV measurement data obtained from a ZPG TBL in a different wind tunnel facility at $Re_\theta = 2770$ ($Re_\tau = 930$, see Fig. 8 in [19]).

In the present measurement configuration the spanwise extension of the structures could not be measured. Multiple-camera (photogrammetric), time-resolved techniques such as tomographic PIV [20] or 3-D PTV [21, 22, 23], or digital holography [24] are ideal candidates to capture the fully resolved velocity field of the small separation bubble.

The presented PIV measurement technique and associated post-processing methods are believed to be valuable tools in the investigation of rare flow phenomena that could not be reliably captured before. While not subject of the present study, the available measurement data also exhibits rare strong wall-normal velocity events very close to the wall that have been investigated through DNS by Lenaers et al [4].

Acknowledgements

The authors would like to acknowledge the financial support provided through the European High performance Infrastructures in Turbulence (EuHIT) Transnational Access Program (European Grant Agreement no. 312278, www.euhit.org). The LML members also acknowledge the regional councils of Nord-Pas-de-Calais, the CNRS and the European Community for providing funding for the refurbishment of the wind tunnel facility through the CISIT project.

References

[1] H. Eckelmann, The structure of the viscous sublayer and the adjacent wall region in a turbulent channel flow, Journal of Fluid Mechanics 65 (1974) 439–459. doi:10.1017/S0022112074001479.
URL http://journals.cambridge.org/article_S0022112074001479

[2] P. Spalart, G. Coleman, Numerical study of a separation bubble with heat transfer, European Journal of Mechanics B - Fluids 16 (2) (1997) 169–189.
URL http://eprints.soton.ac.uk/71967/

[3] Z. Hu, C. L. Morfey, N. D. Sandham, Wall pressure and shear stress spectra from direct simulations of channel flow, AIAA Journal 44 (7) (2006) 1541–1549.
URL https://doi.org/10.2514/1.17638

[4] P. Lenaers, Q. Li, G. Brethouwer, P. Schlatter, R. Örlü, Rare backflow and extreme wall-normal velocity fluctuations in near-wall turbulence, Physics of Fluids 24. doi:10.1063/1.3696304.
URL http://dx.doi.org/10.1063/1.3696304

[5] G. K. E. Khoury, P. Schlatter, G. Brethouwer, A. V. Johansson, Turbulent pipe flow: Statistics, *Re*-dependence, structures and similarities with channel and boundary layer flows, Journal of Physics: Conference Series 506 (1) (2014) 012010. doi:10.1088/1742-6596/506/1/012010.
URL http://stacks.iop.org/1742-6596/506/i=1/a=012010

[6] J. I. Cardesa, J. P. Monty, J. Soria, M. S. Chong, Skin-friction critical points in wall-bounded flows, Journal of Physics: Conference Series 506 (1) (2014) 012009.
URL http://stacks.iop.org/1742-6596/506/i=1/a=012009

[7] R. Vinuesa, R. Örlü, P. Schlatter, Characterisation of backflow events over a wing section, Journal of Turbulence 18 (2) (2017) 170–185. doi:10.1080/14685248.2016.1259626.
URL http://dx.doi.org/10.1080/14685248.2016.1259626

[8] G. Johansson, An experimental study of the structure of a flat plate turbulent boundary layer, using laser-doppler velocimetry, Ph.D. thesis, Chalmers University of Technology, Göteborg, Sweden (1988).

[9] C. Brücker, Evidence of rare backflow and skin-friction critical points in near-wall turbulence using micropillar imaging, Physics of Fluids 27 (3) (2015) –. doi:10.1063/1.4916768.
URL http://dx.doi.org/10.1063/1.4916768

[10] C. E. Willert, High-speed particle image velocimetry for the efficient measurement of turbulence statistics, Experiments in Fluids 56 (1). doi:10.1007/s00348-014-1892-4.
URL http://dx.doi.org/10.1007/s00348-014-1892-4

[11] C. Cuvier, S. Srinath, M. Stanislas, J. M. Foucaut, J. P. Laval, C. J. Kähler, R. Hain, S. Scharnowski, A. Schrder, R. Geisler, J. Agocs, A. Röse, C. Willert, J. Klinner, O. Amili, C. Atkinson, J. Soria, Extensive characterisation of a high reynolds number decelerating boundary layer using advanced optical metrology, Journal of Turbulence 18 (10) (2017) 929–972. doi:10.1080/14685248.2017.1342827.
URL http://dx.doi.org/10.1080/14685248.2017.1342827

[12] J. A. Sillero, J. Jimnez, R. D. Moser, One-point statistics for turbulent wall-bounded flows at reynolds numbers up to $\delta^+ \approx 2000$, Physics of Fluids 25 (10) (2013) –. doi:10.1063/1.4823831.
URL http://scitation.aip.org/content/aip/journal/pof2/25/10/10.1063/1.4823831

[13] G. Eitel-Amor, R. Örlü, P. Schlatter, Simulation and validation of a spatially evolving turbulent boundary layer up to $Re_\theta = 8300$, International Journal of Heat and Fluid Flow 47 (2014) 57–69. doi:{10.1016/j.ijheatfluidflow.2014.02.006}.
URL https://doi.org/10.1016/j.ijheatfluidflow.2014.02.006

[14] K. A. Chauhan, P. A. Monkewitz, H. M. Nagib, Criteria for assessing experiments in zero pressure gradient boundary layers, Fluid Dynamics Research 41 (2) (2009) 021404. doi:10.1088/0169-5983/41/2/021404.
URL http://stacks.iop.org/1873-7005/41/i=2/a=021404

[15] S. Große, W. Schröder, High reynolds number turbulent wind tunnel boundary layer wall-shear stress sensor, Journal of Turbulence 10 (14) (2009) 1–12. doi:10.1080/14685240902953798.
URL http://dx.doi.org/10.1080/14685240902953798

[16] L. Keirsbulck, L. Labraga, M. G. el Hak, Statistical properties of wall shear stress fluctuations in turbulent channel flows, International Journal of Heat and Fluid Flow 37 (0) (2012) 1 – 8. doi:{10.1016/j.ijheatfluidflow.2012.04.004}.
URL http://www.sciencedirect.com/science/article/pii/S0142727X12000537

[17] N. Miyagi, M. Kimura, H. Shoji, A. Saima, C.-M. Ho, S. Tung, Y.-C. Tai, Statistical analysis on wall shear stress of turbulent boundary layer in a channel flow using micro-shear stress imager, International Journal of Heat and Fluid Flow 21 (2000) 576–581. doi:10.1016/S0142-727X(00)00047-3.
URL https://doi.org/10.1016/S0142-727X(00)00047-3

[18] W. Schoppa, F. Hussain, Coherent structure generation in near-wall turbulence, Journal of Fluid Mechanics 453 (2002) 57–108. doi:10.1017/S002211200100667X.
URL http://journals.cambridge.org/article_S002211200100667X

[19] A. Schröder, D. Schanz, R. Geisler, S. Gesemann, C. Willert, Near-wall turbulence characterization using 4D-PTV Shake-The-Box, in: 11th International Symposium on Particle Image Velocimetry PIV15, Santa Barbara (CA), USA, 2015.
URL http://www.piv2015.org/

[20] F. Scarano, Tomographic PIV: principles and practice, Measurement Science and Technology 24 (1). doi:10.1088/0957-0233/24/1/012001.
URL http://stacks.iop.org/0957-0233/24/i=1/a=012001

[21] M. Bross, C. J. Kähler, Time-resolved 3D-PTV analysis of near wall reverse flow events in APG turbulent boundary layers, in: 18th International Symposium on Applications of Lasers and Imaging Techniques to Fluid Mechanics, Lisbon, Portugal, 2016.
URL http://ltces.dem.ist.utl.pt/lxlaser/lxlaser2016/finalworks2016/papers/03.7_3_71paper.pdf

[22] D. Schanz, A. Schröder, S. Gesemann, 'Shake The Box' - a 4D PTV algorithm: Accurate and ghostless reconstruction of lagrangian tracks in densely seeded flows, in: 17th International Symposium on Applications of Laser Techniques to Fluid Mechanics, Lisbon, Portugal, 2014.
URL http://ltces.dem.ist.utl.pt/lxlaser/lxlaser2014/finalworks2014/papers/01.5_5_328paper.pdf

[23] D. Schanz, S. Gesemann, A. Schröder, Shake-The-Box: Lagrangian particle tracking at high particle image densities, Experiments in Fluids 57 (5) (2016) 1–27. doi:10.1007/s00348-016-2157-1.
URL http://dx.doi.org/10.1007/s00348-016-2157-1

[24] J. Sheng, E. Malkiel, J. Katz, Using digital holographic microscopy for simultaneous measurements of 3D near wall velocity and wall shear stress in a turbulent boundary layer, Experiments in Fluids 45 (6) (2008) 1023–1035. doi:10.1007/s00348-008-0524-2.
URL http://dx.doi.org/10.1007/s00348-008-0524-2

a)

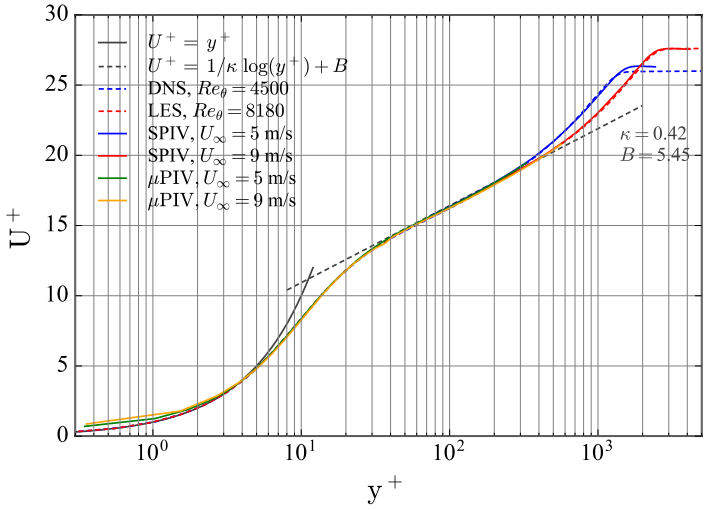

b)

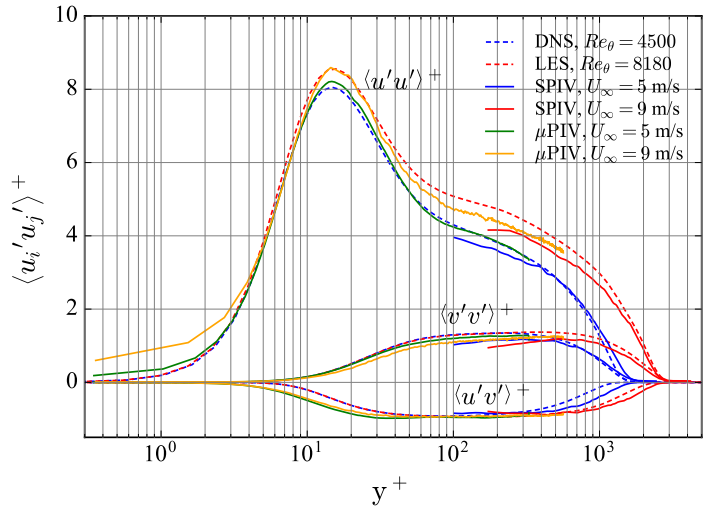

Figure 2: Profiles scaled with inner variables of the mean streamwise velocity (a) and Reynolds stresses (b) for two different free stream velocities obtained $X = 6.8\,\mathrm{m}$ downstream of the tripping device.

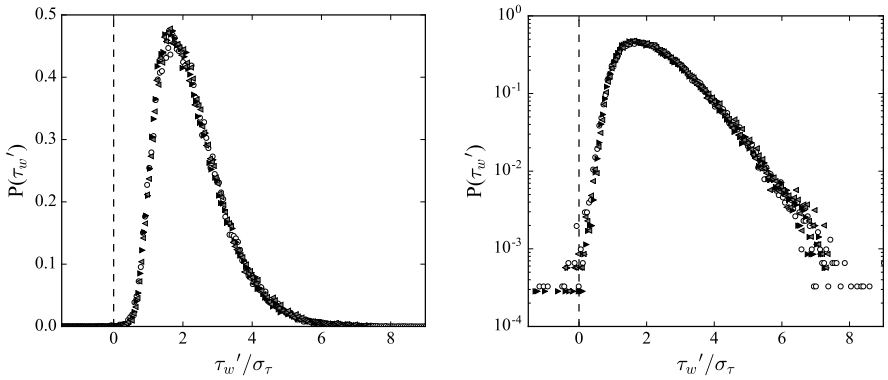

Figure 3: Probability density functions of wall shear stress τ_w for three separate image sequences obtained for $Re_\theta = 4000$ ($X = 3.2\,\mathrm{m}$) in linear (left) and logarithmic scaling (right).

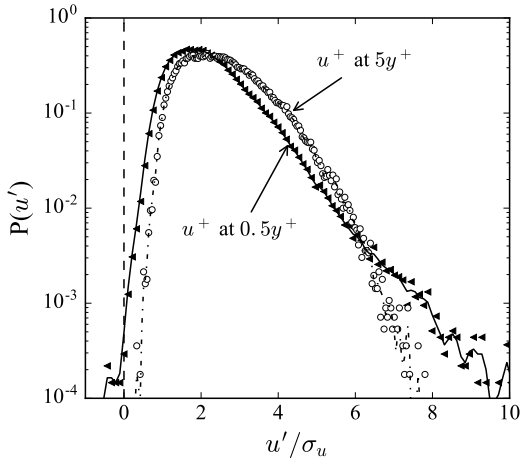

Figure 4: Probability density functions of the fluctuating streamwise velocity u^+ at wall distances of $0.5\,y^+$ and $5\,y^+$ for $Re_\theta = 2537$ ($X = 3.2\,\mathrm{m}$).

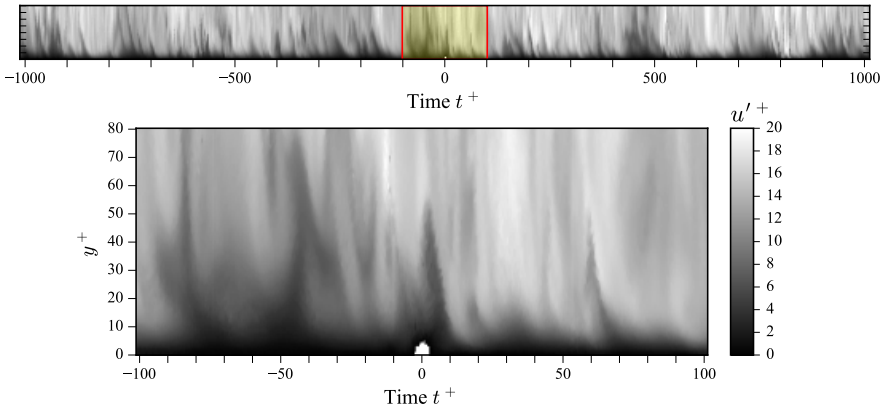

Figure 5: Time trace of streamwise velocity u' at $U_\infty = 5\,\mathrm{m/s}$ ($Re_\theta = 4767$, $X = 6.8\,\mathrm{m}$) covering 0.75 s (5000 samples, top) and 0.075 s (500 samples, bottom). The white region at time $t^+ = 0$ indicates a single reverse flow event. In both sub-plots the vertical axis represents wall distance $0 < y < 80^+$ ($\approx 6\,\mathrm{mm}$).

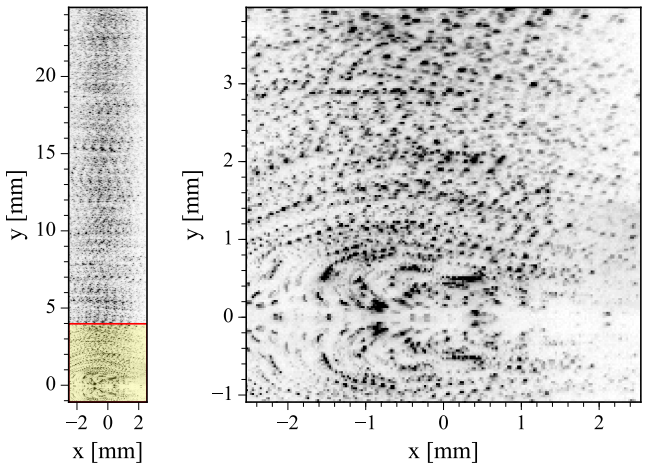

Figure 6: Multi-exposed particle images showing a near wall flow reversal event in a ZPG TBL at $Re_\theta = 4767$ ($X = 6.8\,\mathrm{m}$, $U_\infty = 5\,\mathrm{m/s}$). Full image view at left with detail on right. The tunnel glass wall is located at $Y = 0$ with reflections of particle images visible at $Y < 0$.

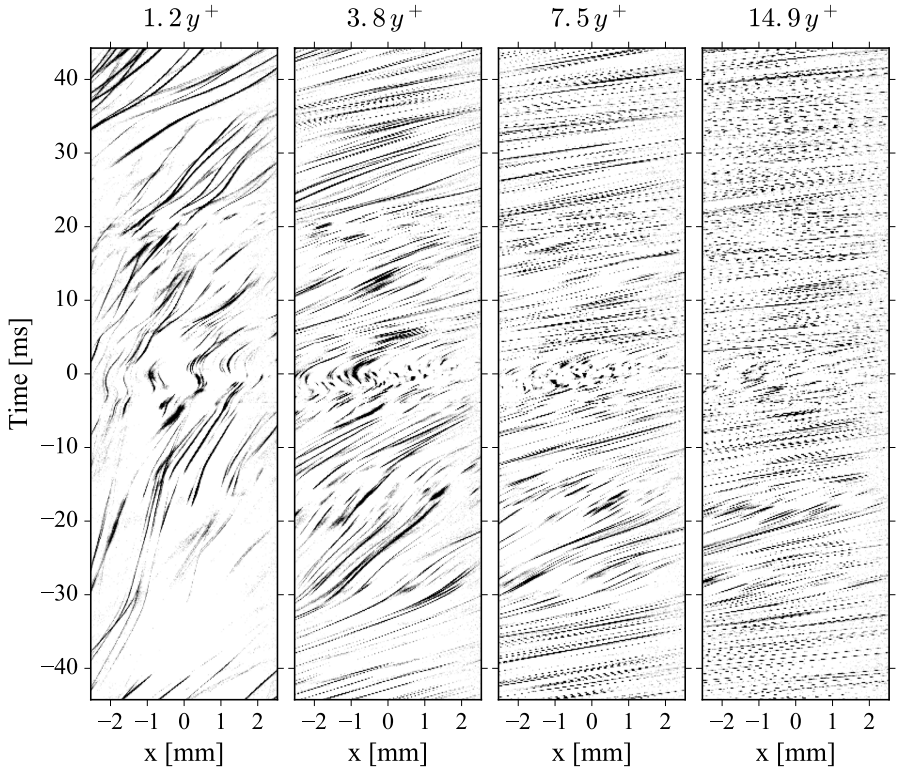

Figure 7: Particle streaks extracted at various wall-normal distances at $U_\infty = 5\,\mathrm{m/s}$ ($Re_\theta = 4767$) covering 0.1 s (667 samples; $274\,t^+$) on vertical axis. A single reverse flow event is located near $t = 0$.

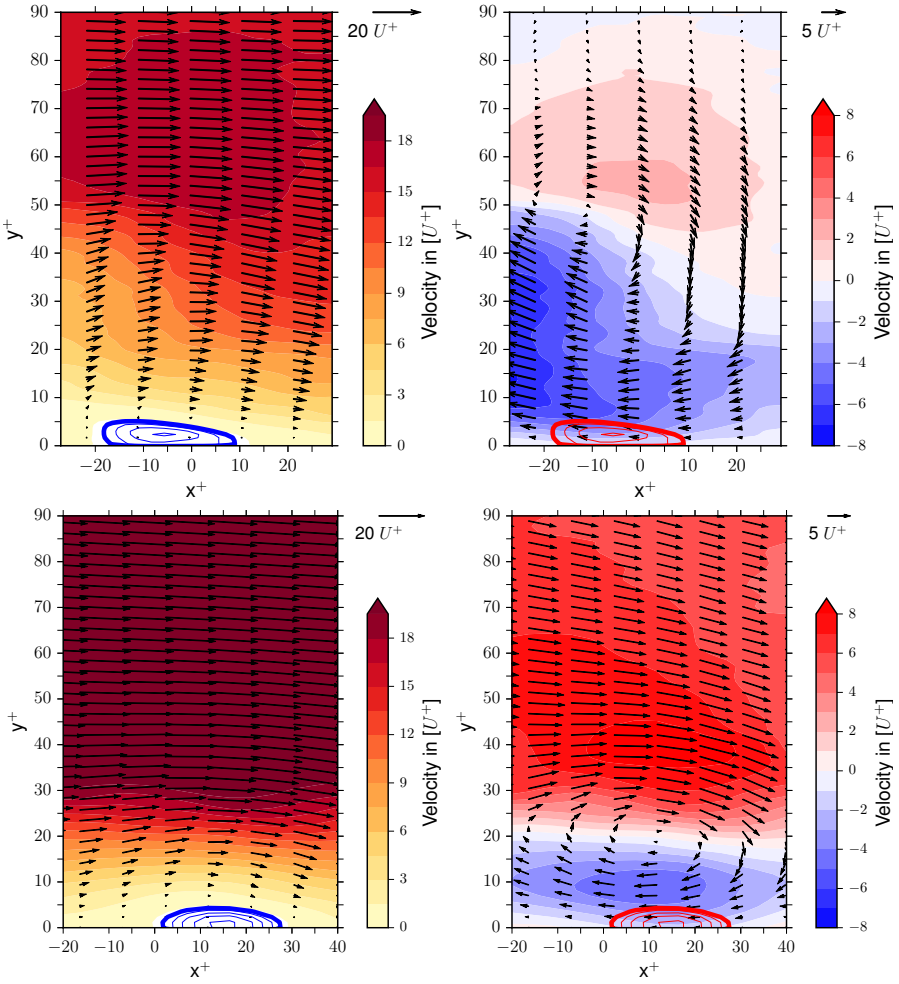

Figure 8: Single reverse flow events at $Re_\theta = 4767$ (top) and $Re_\theta = 7952$ (bottom) shown in viscous scaled units (left) and with mean local streamwise velocity subtracted (right). Contours near $y = 0$ represent horizontal velocity $U \leq 0$ at increments of $0.2U^+$.

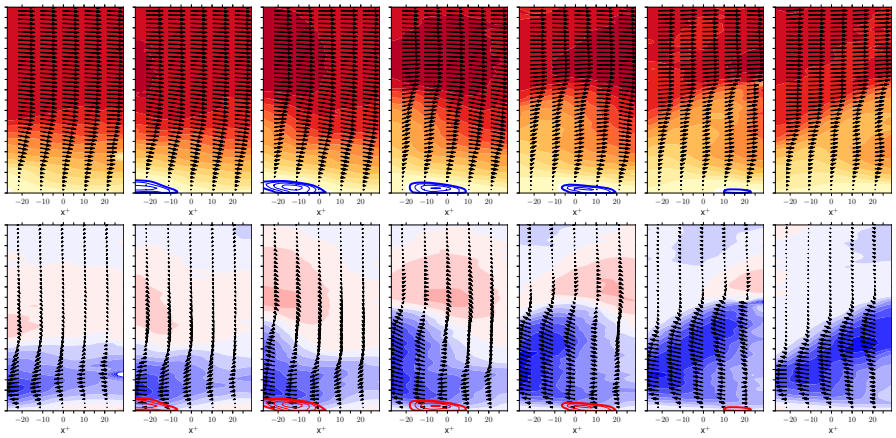

Figure 9: Sequence showing the temporal evolution of a flow reversal event at $Re_\theta = 4767$. Contours, vector and vertical axis scaling as in Fig. 8. Red contour near the wall indicates area of negative streamwise velocity. Temporal separation between frames is $600\,\mu$s; PIV sampling window of 32×8 pixels with 75% overlap, vectors down-sampled $4\times$ horizontally, $3\times$ vertically. Bottom row is plotted in fluctuating velocity (mean local streamwise velocity subtracted).

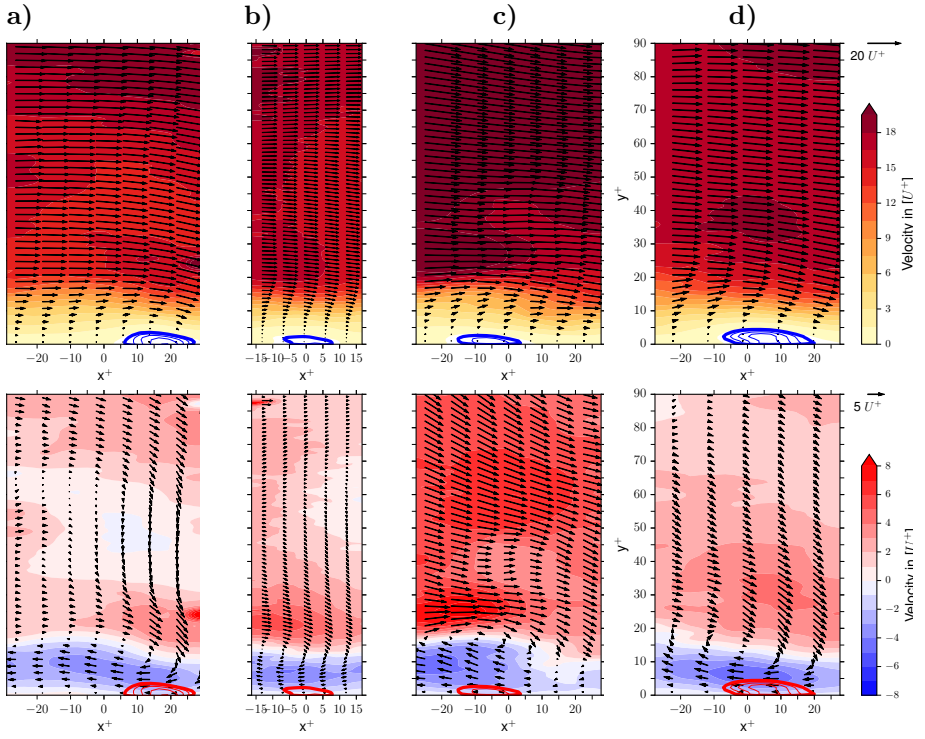

Figure 10: Various instances of near wall reverse flow obtained at measurement position $x = 3.2\,\mathrm{m}$ at $Re_\theta = 2537$ (a,b) and $Re_\theta = 4000$ (c,d). Bottom row is plotted in fluctuating velocity (mean local streamwise velocity subtracted).